Since January 2020 Elsevier has created a COVID-19 resource centre with free information in English and Mandarin on the novel coronavirus COVID-19. The COVID-19 resource centre is hosted on Elsevier Connect, the company's public news and information website.

Matter

CellPress

Article

Integrated contact lens sensor system based on multifunctional ultrathin MoS_2 transistors

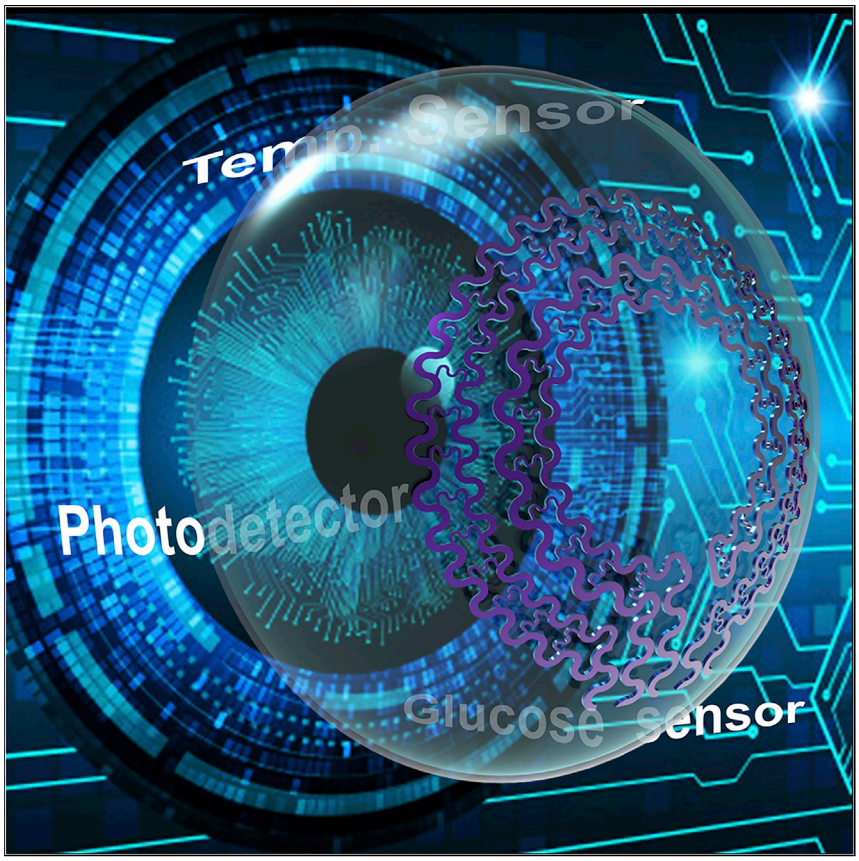

A multifunctional smart contact lens with an ultrathin MoS_2 transistors-based serpentine mesh sensor system was developed, featuring easy assembly, good detection sensitivity, strong robustness, high stretchability, transparency, and full biocompatibility. The integrated sensor systems contain a photodetector for receiving optical information, imaging and vision assistance, a temperature sensor for diagnosing potential corneal disease, and a glucose sensor for monitoring glucose levels directly from the tear fluid.

Shiqi Guo, Kaijin Wu, Chengpan Li, ..., Fernando A. Castro, Dong Yang, Yunlong Zhao

wsyangdong@gmail.com (D.Y.)
yunlong.zhao@surrey.ac.uk (Y.Z.)

Highlights

Smart contact lenses integrate photodetectors, glucose sensors, and temperature sensors

Ultrathin serpentine mesh sensor layer can be directly mounted onto the contact lens

Sensor layer directly contacts with tears and does not interfere with blinking or vision

It shows high detection sensitivity, good biocompatibility, and mechanical robustness

4 **Demonstrate**
Proof-of-concept of performance with intended application/response

Guo et al., Matter 4, 969–985
March 3, 2021
https://doi.org/10.1016/j.matt.2020.12.002

Matter

CellPress

Article

Integrated contact lens sensor system based on multifunctional ultrathin MoS_2 transistors

Shiqi Guo,[1,9] Kaijin Wu,[2,9] Chengpan Li,[3] Hao Wang,[4] Zheng Sun,[5] Dawei Xi,[1] Sheng Zhang,[6] Weiping Ding,[3] Mona E. Zaghloul,[5] Changning Wang,[4] Fernando A. Castro,[7,8] Dong Yang,[4,9,*] and Yunlong Zhao[7,8,10,*]

Summary

Smart contact lenses attract extensive interests due to their capability of directly monitoring physiological and ambient information. However, previous demonstrations usually lacked efficient sensor modalities, facile fabrication process, mechanical stability, or biocompatibility. Here, we demonstrate a flexible approach for fabrication of multifunctional smart contact lenses with an ultrathin MoS_2 transistors-based serpentine mesh sensor system. The integrated sensor systems contain a photodetector for receiving optical information, a glucose sensor for monitoring glucose level directly from tear fluid, and a temperature sensor for diagnosing potential corneal disease. Unlike traditional sensors and circuit chips sandwiched in the lens substrate, this serpentine mesh sensor system can be directly mounted onto the lenses and maintain direct contact with tears, delivering high detection sensitivity, while being mechanically robust and not interfering with either blinking or vision. Furthermore, the *in vitro* cytotoxicity tests reveal good biocompatibility, thus holding promise as next-generation soft electronics for healthcare and medical applications.

Introduction

The enormous impact of the coronavirus disease 2019 (COVID-19) pandemic, together with other diseases or chronic health risks has significantly prompted the development and application of bioelectronics and medical devices for real-time monitoring and diagnosing health status.[1–5] Stretchable and flexible devices worn on or implanted in the human body with embedded multifunctional biosensors should enable real-time sensing of physiological signals (e.g., heart rate, body temperature, oxygen saturation) and/or ambient conditions (e.g., the surrounding temperature, humidity, and light and audio levels) without affecting the normal body movements.[6–13] By integrating and analyzing a large amount of live data, these devices could dramatically enhance the efficiency of healthcare delivery and carry out delivery of medicines more timely, personalized, and precise.[14–18] Among all these devices, contact lenses are one of the most popular wearable devices, designed for vision correction, and aesthetic and therapeutic purposes.[19–23] They are in direct contact with both internal chemistry from tear fluid and eyeball and external air for hours without serious irritation, which can provide a unique platform for continuous interrogation of both physiological information and ambient conditions. Taking the diabetic diagnostics as an example, to collect accurate data with non- or minimally invasive techniques, the glucose level tends to be tested from the "open" body fluids rather than blood.[23] Multipatient clinical trials have demonstrated clearly

Progress and potential

Wearable smart contact lenses have attracted extensive interests because of their ability to monitor physiological information and ambient information directly from eyeball and body fluids. However, conventional smart contact lens systems lack efficient sensor modalities, facile fabrication process, mechanical stability, or biocompatibility. This study develops a multifunctional, high-transparency and easy-access smart contact lens system. Specifically, the serpentine mesh sensor system can be directly mounted onto the lens substrate and maintain direct contact with tears, delivering high detection sensitivity, while being mechanically robust and not interfering with either blinking or vision. This integrated contact lens sensor system and fabrication strategy allows for easy incorporation of other functional components, such as an electrode array for electroretinography, antennas for wireless communication, and power modules for future *in vivo* exploration.

that tear fluid can be a valuable marker for measurements of systemic glucose.[24] Smart contact lenses equipped with high sensitivity glucose sensors could open the possibility of a non-invasive method to continuously detect biomarkers in tears.[25–29] Owing to the abundant proteins or biomarkers from tear fluid, smart contact lenses are expected to provide higher accuracy/reliability of the resulting data in comparison with the analyses from skin or sweat by other conventional wrist-worn watches or smart patches. Although controversy may remain, recent studies have shown that the blood glucose concentrations estimated with the tear glucose concentrations obtained by glucose sensors exhibit a high correlation with those actually measured with a clinically available glucometer ($R^2 = 0.9617$).[30] As complications of diabetes, stroke, and heart disease are also closely related to disorders of blood glucose regulation; these disorders could also increase the risk of high blood pressure, lower limb nerve damage, kidney diseases, and retina injury.[31–33] Meanwhile, monitoring the intraocular and extraocular environment helps to provide a database to diagnose and treat ocular diseases. For example, embedded photodetectors on the lenses are capable of potentially monitoring the light intensity, testing and utilizing eye blinking, receiving optical data, and assisting vision.[27] Embedded temperature sensors could be used for monitoring corneal temperature, tracking of intraocular pressure,[34] and providing information for ocular disease, such as diagnosing dry eye disease[35] and inflammation.[36] Monitoring ocular temperature after ophthalmic surgery also has clinical significance in case of postoperative infection.[35] The smart contact lenses could also be equipped with application-specific integrated circuit chips,[26] multiple electrode arrays,[37,38] or antenna[25,39] to further enrich their functionality to obtain, process, and transmit physiological properties, manage illnesses and health risks, and finally promote health and wellbeing.

Despite significant efforts, use of smart contact lenses remains limited because of their mechanical biocompatibility, detection sensitivity, and challenging integration process.[20,40] Many characteristics are required for the successful development of smart contact lenses. Firstly, they should not only have a high degree of transparency in visual field but also be comfortable to wear. To minimize the potential for inflammation and irritation, the embedded sensors or circuit chips should be fully stable, biocompatible, and have negligible mechanical stiffness relative to the eyeball. Flexible and transparent ultrathin electronic materials, e.g., mono- to few-layered 2D transition metal dichalcogenide (TMDC),[41–45] could be the ideal building blocks for this purpose, although the difficulty remains in the choice of the specific materials and manufacturing process. Also, unlike traditional rigid or bulk sensors and circuit chips that are sandwiched in the lens substrate and contacted with tear fluid via microfluidic sensing channels,[46–48] the ultrathin sensors could directly stick onto the lenses and contact the tear fluid, yielding a better detection sensitivity and easier assembly without interfering with blinking.

To achieve the above goals, in this work, soft contact lenses with multifunctional sensor systems were fabricated using ultrathin (few-to-monolayer) TMDC semiconductors, elastic interconnect electrodes, polyimide (PI) passivation layers, and a polydimethylsiloxane (PDMS) lens substrate. Here, we chose MoS_2 transistors as the core sensing material because of their large surface-to-volume ratio, layered dangling-bond-free surface, tunable bandgap and charge transfer properties, and good biocompatibility.[13,49–57] Unlike traditional top-down fabrication[58,59] and bottom-up synthesis methods,[60–62] we applied a gold-mediated exfoliation[63] and assembly strategy (Figure 1A) to pattern mono-to-few-layered MoS_2 flakes with large lateral size (~200 × 100 μm). The MoS_2 transistors were mechanically reinforced with a thin layer of photo-patternable PI, while the elastic parts were formed using a

[1]John A. Paulson School of Engineering and Applied Sciences, Harvard University, Cambridge, MA 02138, USA

[2]CAS Key Laboratory of Mechanical Behavior and Design of Materials, Department of Modern Mechanics, CAS Center for Excellence in Complex System Mechanics, University of Science and Technology of China, Hefei, Anhui 230026, China

[3]Department of Electronic Science and Technology, University of Science and Technology of China, Hefei, Anhui 230027, China

[4]Athioula A. Martins Center for Biomedical Imaging, Department of Radiology, Massachusetts General Hospital, Harvard Medical School, Charlestown, MA 02129, USA

[5]School of Engineering and Applied Science, The George Washington University, Washington, DC 20052, USA

[6]Ningbo Research Institute, Zhejiang University, Zhejiang, Ningbo 315100, China

[7]Advanced Technology Institute, University of Surrey, Guildford, Surrey GU2 7XH, UK

[8]National Physical Laboratory, Teddington, Middlesex TW11 0LW, UK

[9]These authors contributed equally

[10]Lead contact

*Correspondence: wsyangdong@gmail.com (D.Y.), yunlong.zhao@surrey.ac.uk (Y.Z.)

https://doi.org/10.1016/j.matt.2020.12.002

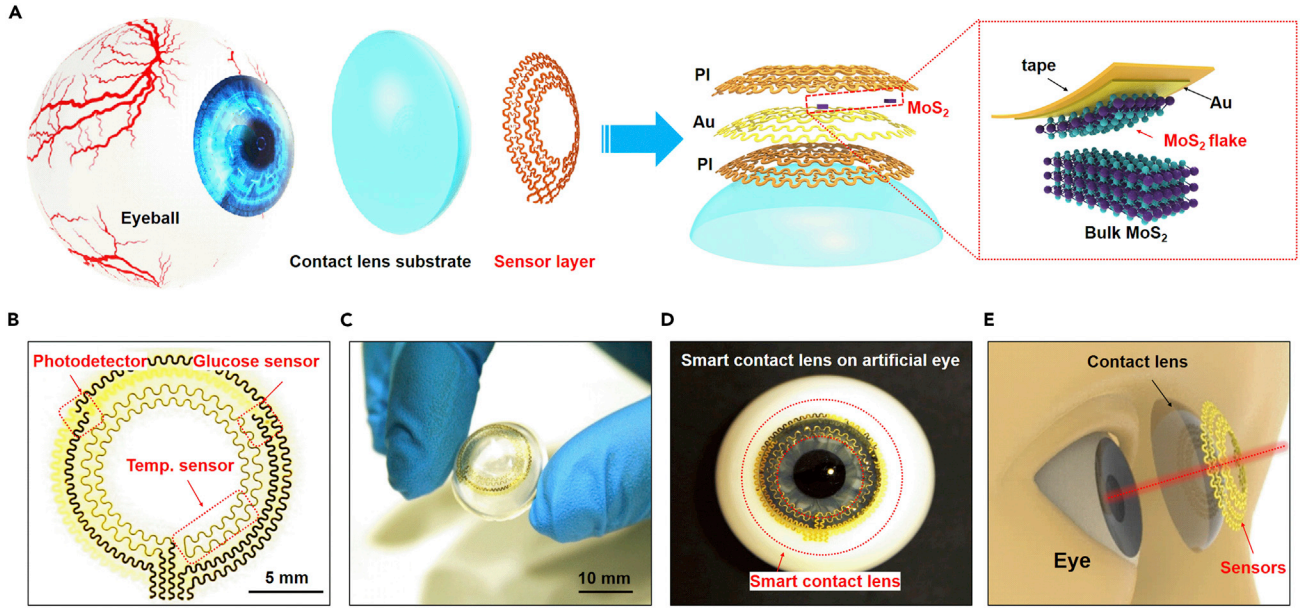

Figure 1. Structural design of a smart contact lens with ultrathin MoS_2 transistors-based serpentine mesh sensor system

(A) Schematic illustration of the different layers of smart contact lens structure attached to an eyeball. The dashed region highlights the gold-mediated mechanical exfoliation of monolayer MoS_2.

(B) Optical image of the serpentine electrode and sensor structure.

(C) Photograph of the sensor layer transferred onto a dome-shaped PDMS substrate.

(D) Photograph of the system placed on an artificial eye.

(E) Illustration of the smart contact lens and the corresponding dimensions with human eyes.

serpentine gold (Au) and PI mesh structure. The sensor system is placed around the outer ring of the cornea to avoid blocking vision (Figure 1B). Such a design can effectively protect electronics from destructive mechanical deformations while maintaining high flexibility/stretchability and can easily convert functional components into various shapes of curvatures, which was verified by mechanical analysis. The integrated sensor system allows the collection of optical, glucose, and temperature information from the contact lens. The ultrathin MoS_2 transistors exhibit a high sensitivity (<0.1 mM) for glucose monitoring, a fast response (<1 s), high current on/off ratio (>10^3 with UV illumination), and high responsivity (4.8 A/W) for photodetection; while the temperature sensor made of Au wires yields a precise measurement of temperature even when highly stretched. In addition, we examined the light absorption of the entire contact lens to demonstrate its transparency and conducted *in vitro* cytotoxicity tests to confirm its biocompatibility. Taken together, our material and device characteristics demonstrate that the requirements for practical applications have been well fulfilled by such a contact lens, providing a novel and facile approach for multifunctional contact lens sensor systems.

Results and discussion

Structural design of the smart contact lens

Figure 1A illustrates the layout and the overall structure of the smart contact lens, comprising a donut-shaped sensor layer and a PDMS lens substrate attached to the eyeball. In the sensor layer, hybrid sensors with a serpentine interconnect of Au electrodes (150 nm) are passivated or supported in a single-layer manner by the thin PI layer(s) (2.5 μm per layer) (Figure 1A, right). This serpentine mesh structure provides not only good flexibility and stretchability but also maintains a neutral

mechanical plane for keeping the uniaxial strain close to zero when the structure bends slightly.[64–66] The sensor layer is composed of a MoS_2 photodetector, a MoS_2 glucose sensor, and a Au temperature sensor, each interconnected by a pair of serpentine metal electrodes (Figure 1B). The photograph in Figure 1C displays the sensor layer on top of a dome-shaped PDMS substrate (30 μm), featuring good adhesion and bonding to the surface. As the most widely used silicon-based organic polymer, PDMS has been broadly applied as the substrate in diverse biomedical fields, including contact lenses.[67,68] Compared with other commercial materials used in contact lenses (e.g., polymethyl methacrylate, polyvinyl acetate, rigid gas-permeable materials, and hydrogels), PDMS is inexpensive, easily manufactured, durable, comfortable to wear, and exhibits high oxygen permeability;[69,70] the main disadvantage of low hydrophilicity could be mitigated by plasma treatment, hydrophilic polymer grafting, or surface modification with embedded surfactants[71] (Table S1). Figure 1D shows a photograph of the smart lens on an artificial eye, indicating that the pupil is not covered by the sensors and therefore that the electrode will not block vision (Figure 1E).

Fabrication and structural characterization of the smart contact lens

In our design, the large-area ultrathin MoS_2 flake transistors are used for photodetection and glucose sensing. To obtain the key materials, traditional mechanical exfoliation has been widely applied (Figure S1), but often limited by the small size (<1,000 μm^2), low yield with uncontrollable thickness, and electrical performance. To overcome this limitation, a gold-mediated exfoliation method[63] was used. As shown in Figure 2A, a Au film (120 nm) was electron-beam evaporated on top of the MoS_2 bulk materials to help detach the topmost layer from the bulk. The topmost layer of MoS_2 was peeled off using a thermal release tape, which was later released with heat after transferring the MoS_2 to a target substrate. After Au etching, large-area MoS_2 flakes were obtained for further assembly. Figure 2B shows a representative optical image of a gold-mediated exfoliated MoS_2 flake with a lateral size of ~200 × 100 μm. A Raman spectrum of the obtained MoS_2 flakes presents the A_{1g} mode at 408 cm^{-1} and the E^1_{2g} mode at 385 cm^{-1} (Figure 2C), in agreement with the typical vibration modes of MoS_2.[72] A high-resolution transmission electron microscopy (TEM) image shows the ultrathin layered structure with a lattice spacing of 0.27 nm, corresponding to the (101) interplanar distance of MoS_2 (Figure 2D). The MoS_2 flakes exfoliated by this method are mostly monolayers, except for some that are "few-layers" (<5 layers). A representative atomic force microscope (AFM) image in Figure S2 shows the typical thickness of 1.8 nm for few-layers. To demonstrate the large area size of the gold-mediated exfoliation over the traditional mechanical exfoliation method, we counted 100 flakes of both types and calculated their area sizes. The histograms show that the area size of MoS_2 flakes obtained using this method (Figure 2E, bottom) is two orders of magnitude larger than that using the traditional method (Figure 2E, upper).

To quickly optimize the device configuration, MoS_2 field-effect transistors (FETs) with a basic back-gate configuration were fabricated directly on a SiO_2/Si substrate using a standard nanofabrication process without any other surface functionalization or dielectric coating (Figures 2F, 2G, and S3). The Ti/Au contacts (5 nm/150 nm) on top of MoS_2 work as the source and drain electrodes, while the SiO_2 (285 nm) underneath serves as the gate dielectric (Figure 2F). The highly p-doped silicon substrate, serving as the back-gate electrode, is connected with silver paste. As displayed in the optical image (Figure 2G), the exfoliated MoS_2 flake is capable of hosting several FETs with different channel lengths, providing a platform for optimizing device configuration. Typical output characteristics (I_{DS} versus V_{DS}) (Figure 2H) illustrate

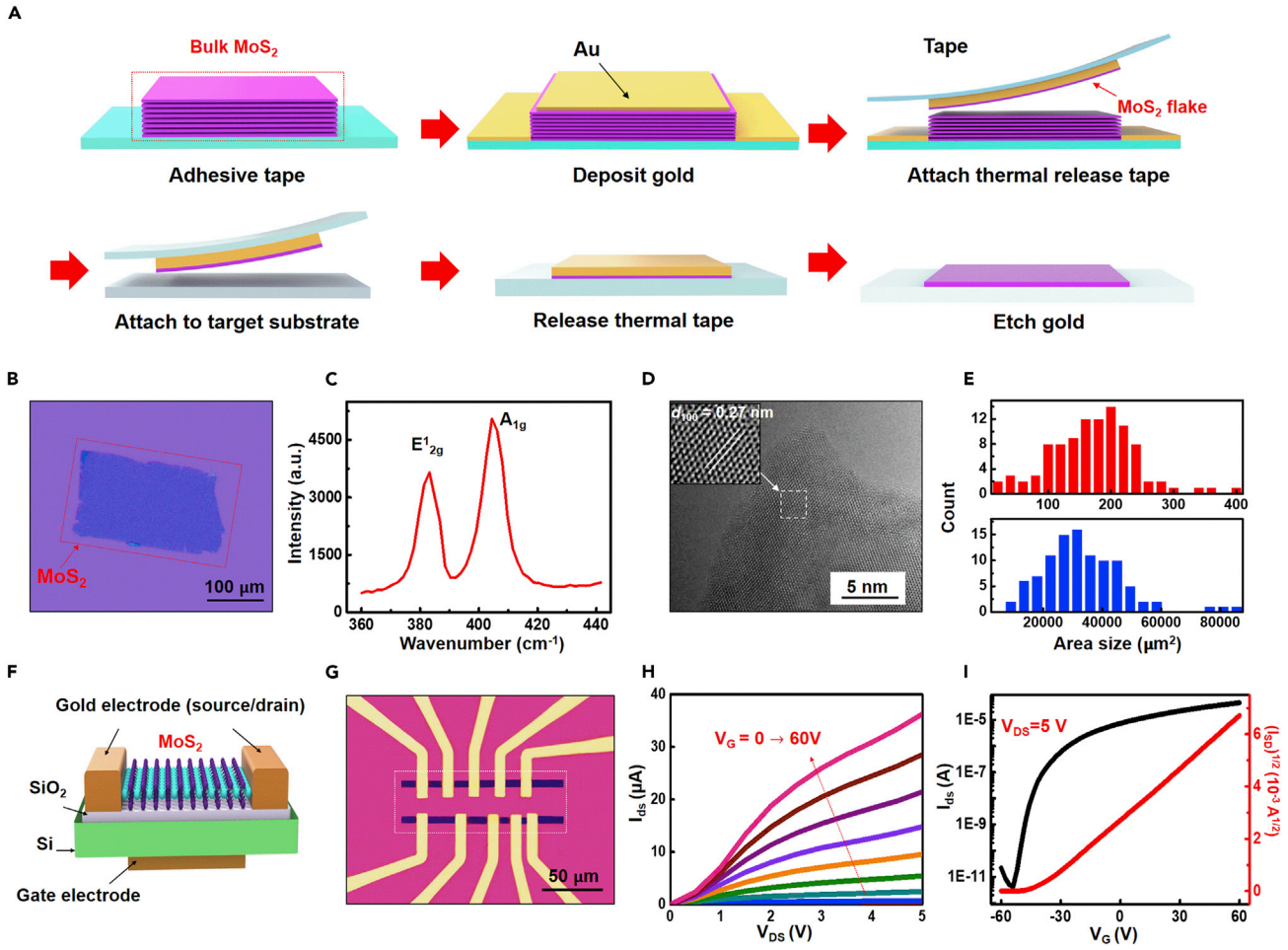

Figure 2. Transfer process and characterization of an exfoliated large-area MoS_2 flake transistor

(A) Schematic illustration of the gold-mediated exfoliation process.

(B) Optical image of an exfoliated MoS_2 flake with a lateral size of ~200 × 100 μm on a SiO_2/Si substrate.

(C) Room-temperature Raman spectrum of MoS_2 showing the A_{1g} mode at 408 cm^{-1} and the $E^1{}_{2g}$ mode at 385 cm^{-1}.

(D) High-resolution TEM image of the atomic layer of MoS_2. Inset is the zoom-in view exhibiting a lattice d100 of 0.27 nm.

(E) Histogram comparing flake area size between traditional mechanical exfoliation (in red) and the gold-assisted exfoliation method (in blue).

(F) 3D schematics of the back-gated FET device on the SiO_2/Si substrate.

(G) Optical image of the MoS_2 FET device from the top. Different channel lengths were fabricated for optimization of the design.

(H) Output curve (source-drain current I_{DS} versus source-drain voltage V_{DS}) with the back-gate voltage V_G sweep from 0 to 60 V.

(I) Transfer curve (I_{DS} as a function of V_G) with V_{DS} = 5 V, shows n-type behavior with an on/off ratio of 10^7.

the MoS_2 FETs with an increasing V_G from 0 to 60 V in steps of 6 V. The transfer curves (I_{DS} versus V_G, black for log scale, red for linear scale) at V_{DS} = 5 V (Figure 2I) exhibit the n-type property with an ON/OFF ratio exceeding 10^7. The field-effect mobility can be extracted with the equation: $\mu_{FE} = \frac{\Delta I_{ds}}{\Delta V_G}\frac{L}{W}\frac{1}{V_{DS}}\frac{1}{C_{ox}}$, where L and W are channel length and channel width. The device displays ON currents of 10 μA μm^{-1} at V_{DS} = 5 V with a field-effect mobility of 9.18 cm^2/Vs, which agree with the reported parameters of monolayer MoS_2 FETs using same or similar device configuration,[50,73,74] while use of a top-gate configuration, or with additional surface functionalization or coating, could further exhibit superior performance.[75] In our experiment, pure gold with high biocompatibility was deposited on the surface of MoS_2 and used as the transfer layer, which can eliminate biologically toxic components or other

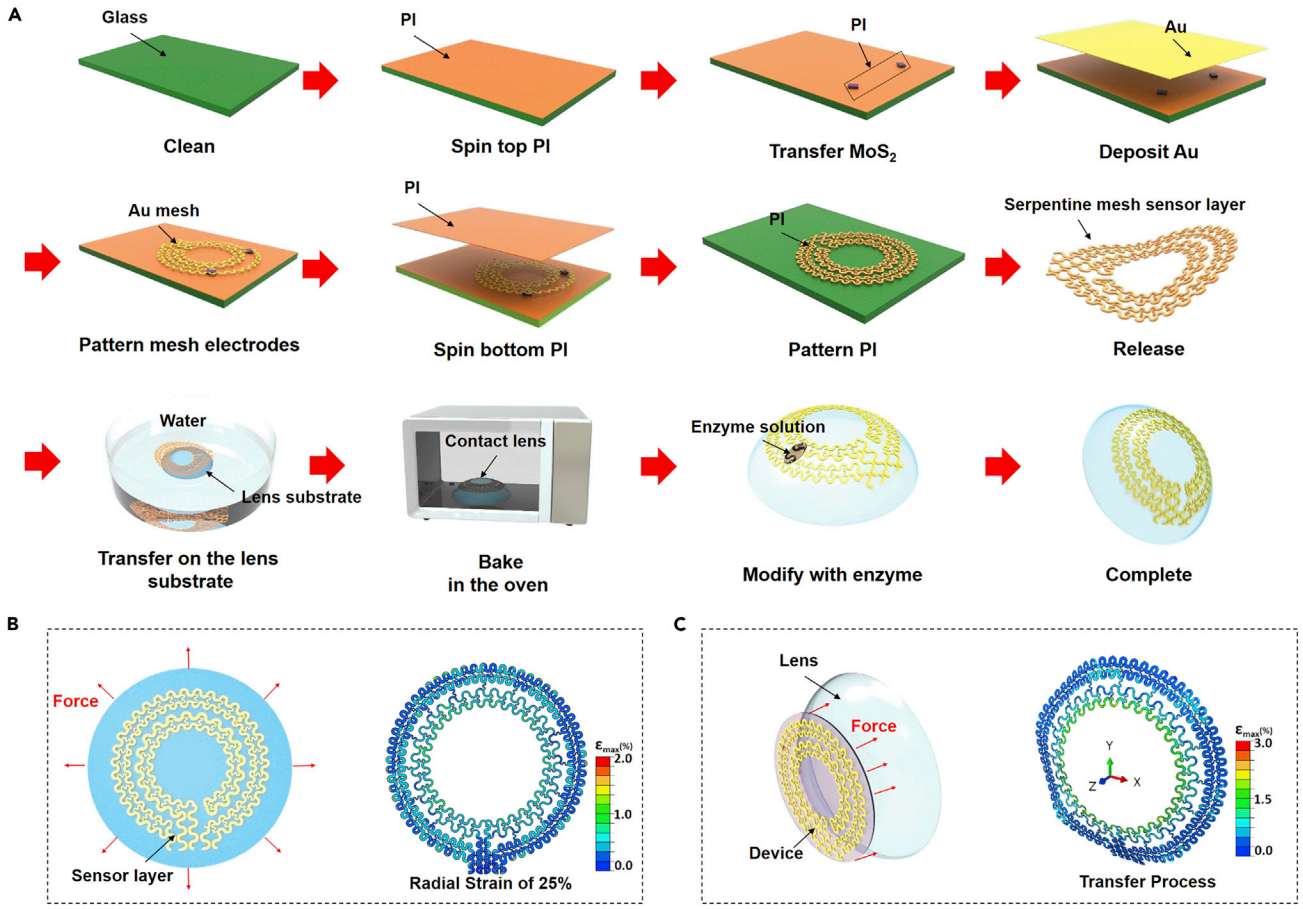

Figure 3. The "pattern-release-transfer" process and mechanical analysis of a smart contact lens

(A) Illustration of the fabrication process of a smart contact lens. We began by coating the bottom PI layer on a glass substrate. The MoS_2 and gold mesh electrodes were consecutively placed and patterned to form the sensor and the interconnect layer. Subsequently, the top PI layer was coated and patterned, followed by release from the glass substrate. Finally, the device was picked up by the PDMS contact lens, oven baked, and enzyme modified to complete the process.

(B) Illustration for the sensor layer with the radial strain (x, y axis) (left) and the FEA strain map under a radial strain of 25% (right).

(C) Illustration of the sensor layer with the longitudinal strain on the perpendicular plane (z axis) (left) and the FEA strain map with 4 mm of z axis displacement (right).

obvious surface contaminants.[76] Overall, the gold-mediated exfoliated MoS_2 exhibits suitably high performance for application as transistors.

With the confirmation of the use of high-performance large-area ultrathin MoS_2 transistors, we fabricated a hybrid, soft, smart contact lens with the key steps of "pattern-release-transfer" (Figure 3A). The entire procedure started with spin-coating PI (~2.5 μm) onto a clean glass substrate as a bottom supporting layer, which was further cured at 150°C for 10 min followed by 250°C for 1 h. The exfoliated MoS_2 flakes were transferred onto the PI layer through a standard printing process with a PDMS stamp[77] (see the equipment in Figure S4), followed by patterning with a thin Cr mask (5 nm) and SF_6/O_2 reactive-ion etching (RIE). A thin Au layer (150 nm) was electron-beam evaporated and patterned on the PI to form a functional Au mesh with a serpentine structure. A top passivation layer of PI was further spin coated with the same thickness (~2.5 μm), cured, and patterned with oxygen plasma. The patterned geometries for two layers of PI match with those of the metal traces,

which places the metal in a mechanically neutral plane while keeping sensors exposed. Finally, the entire sensor layer was cleaned and chemically released with buffered oxide etchant. This process can readily implement flexible and stretchable electronics on elastomeric substrates or curved surfaces. A PDMS contact lens substrate was baked and cured into a dome shape with two enclosed stainless-steel hollow hemispheres. To form a functional contact lens, we developed a physically adhesive strategy that allows the sensor layer to be accurately and firmly attached to the contact lens substrate. The sensor layer was first floated in deionized (DI) water and picked up by a lens substrate from the water (Figure S5). The width and radius of the serpentine mesh structure were rationally designed to match the curvature of the lens substrate perfectly for precise transfer. To ensure good adhesion between the sensor layer and the substrate, the entire lens was baked in a vacuum oven at 60°C for 30 min for dehydration and bubble release. To avoid the enzyme losing its efficacy, the device was kept dry, and finally treated with the glucose-sensing enzyme solution before use. Details of all other dimensions of the entire system are shown in Figure S6.

In the process of transferring or wearing the contact lenses, curvature-induced stress and deformation may occur due to external forces or a geometric mismatch between the lens and the eyeball. Therefore, strain in the radial and longitudinal direction is possible, which may cause local buckling if the stress is larger than the critical buckling load. To understand the mechanical properties and verify the robustness of our design, we performed a finite element analysis (FEA) that showed the strain distribution of the sensor layer on the contact lens under different forces or deformations (Figures 3B and 3C) (see detailed FEA models in the Experimental procedures). Here, all the initial parameters were selected after consideration of the design and practical applications; the maximum tensile and deformation set here has far exceeded the normal operating range of contact lenses. When the sensor layer is placed under symmetrical radial strain from 5% to 25% (Figures 3B and S7) in a plane surface (x, y axes) or uniaxial tensile (x axis, Figure S8; y axis, Figure S9), the maximum principal strains are below 2.0%, lower than the fracture strain of gold film (~7%). The calculated strains in the outer electrode region, where MoS_2 is situated, are below 0.5%, significantly lower than the fracture strain of MoS_2 (~20%). Because the stretching is mainly absorbed by the deformations of serpentine interconnects, no mechanical fracture is expected on the device. When the sensor layer is placed under a longitudinal strain on the perpendicular plane (z axis) with a displacement from 0 to 4 mm (Figures 3C and S10), the maximum principal strains remain <3.0% and the strain in the regions with MoS_2 remains below 0.5%.

We also investigated the mechanical properties of the smart contact lens when attached to an artificial eyeball (Figures S11A and S11B) to simulate operational use. Simulating the movement of the eyeball resulted in only up to 0.5 mm Z displacement with less than 1% strain in the serpentine interconnects, and <0.3% strain in the key sensing region (MoS_2 and Au) (Figure S11C). These results show that all of the architecture of the serpentine mesh interconnects;[78] the PI support layers dominate the mechanical performance of the devices, resulting in a low strain at key functional regions of devices when the substrate is under extreme deformation.,[64,79–81] indicating the strong robustness of the device.

Characterization of the multifunctional sensor system

The multifunctional sensor system is composed of a photodetector, a glucose sensor, a temperature sensor, and with five interconnects where the MoS_2-based photodetector and glucose sensor share one common source electrode and record

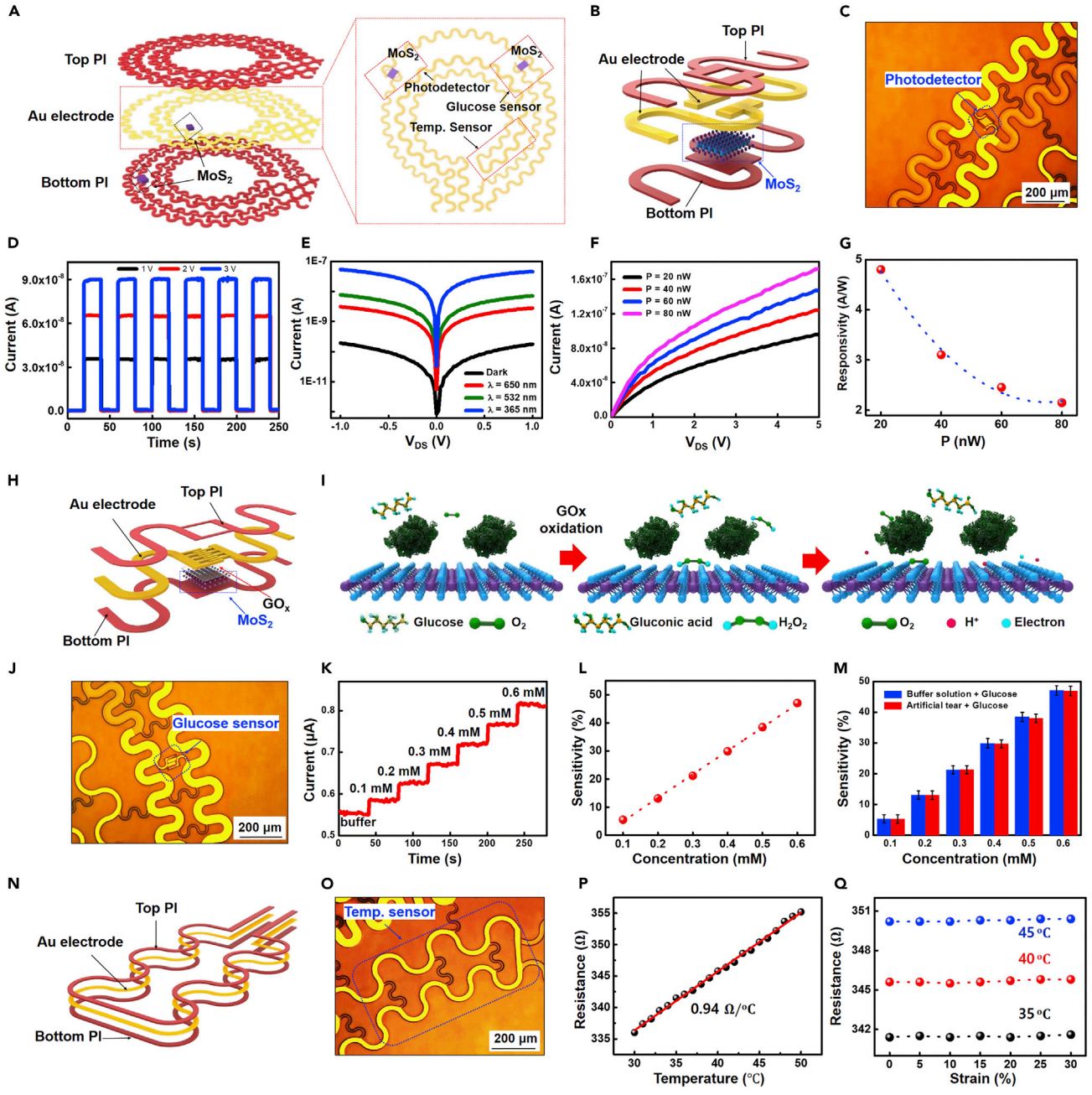

Figure 4. The characteristics of the multifunctional sensor system

(A) Schematic illustration of the multifunctional sensor structure.

(B and C) 3D schematic illustration (B) and optical image (C) of the two-terminal MoS_2 photodetector.

(D) Photoswitching behavior under pulsed illumination by 365 nm wavelength UV light with different V_{DS} values.

(E) Drain-source characteristics in the dark and under illumination with different wavelengths of light.

(F) Drain-source characteristics of the photodetector under different illuminating light intensities.

(G) The photoresponsivity of the MoS_2 phototransistor, exhibiting a high photoresponsivity of 4.8 A/W for a UV power of 20 nW.

(H) Schematic illustration of ac MoS_2 glucose sensor.

(I) Illustration of the sensing mechanism of the device with oxidation of glucose.

(J) Optical image of the MoS_2 glucose sensor.

(K) Time versus current curve based on changes in glucose levels.

(L) The sensitivity ($|\Delta R|/R_0$) of the glucose sensor with a buffer solution, where R_0 is the initial resistance at zero glucose concentration.

Figure 4. *Continued*
(M) Sensitivity of the sensors with the PBS buffer solution (blue) and the artificial tear solution (red). Five devices with each solution were tested and the standard deviation is represented by error bars.
(N and O) Schematic illustration (N) and optical image (O) of the temperature sensor.
(P) The temperature-dependent resistance curve for the Au thermal resistor.
(Q) The resistance of the temperature sensor versus strain under different temperatures.

signals independently by separated drain electrodes (Figure 4A). The sensor system was tested after being connected with an external print circuit board through an anisotropic conductive film cable (Figure S12). Figure 4B gives a 3D schematic view of the photodetector with a large-top PI open window, and with 180 μm channel length for higher photosensitivity. The corresponding optical image is shown in Figure 4C. The photodetector was first characterized under pulsed illumination using a 365 nm wavelength UV light with an intensity of 4 nW under different V_{DS} values (1 V, 2 V, and 3 V, Figure 4D). When the device is illuminated, it exhibits an increase of two orders of magnitude in photocurrent I_{ph} ($I_{ph} = I_{on} - I_{off}$, where I_{on} and I_{off} are the current under illumination and in the dark, respectively) and fast rise time (~50 ms) and fall time (~50 ms) (see magnified plot in Figure S13), indicating excellent photosensitivity and fast response to light illumination. This is enabled by the mechanism illustrated in Figure S14: the illumination can excite electrons from the valence to the conduction band and thus generate photocurrent under source-drain bias. The I_{ph} increases with higher V_{DS} values due to the faster carrier drift velocity. Research and studies claim that light or electromagnetic radiation can result in eye damage through various mechanisms, including photothermal, photomechanical, and photochemical mechanisms.[82] Due to the demand of monitoring light harmful to the retina and of preventing light-induced retinal diseases caused by UV light and short high energy visible light (λ = 320–450 nm),[83,84] we tested our device under different light wavelengths and illumination intensities (Figures 4E–4G). Figure 4E illustrates the I_{DS} versus V_{DS} curve under red laser light (λ = 650 nm), green laser light (λ = 532 nm), and UV light (λ = 365 nm) with the same intensity (5 nW). The I_{ph} at the wavelength of 650 nm is smaller than that at 532 nm and further than 365 nm, indicating a higher transition probability with a shorter excitation wavelength. The optical response and photoresponsivity were further investigated under different UV illumination intensities (20–80 nW) at V_{DS} = 5 V (Figures 4F and 4G). Here, the photoresponsivity R is defined as the ratio of the photocurrent I_{ph} and the incident power P_0: $R = \frac{I_{ph}}{P_0}$.[85] The I_{ph} is increased from 96 to 172 nA, with the intensity increasing from 20 to 80 nW, and R exhibiting very high responsivity for photodetection from 4.8 to 2.15 A/W. The decrease in R with intensity increase is due to the loss of photoexcited carriers by recombination effects, which is commonly observed in TMDC,[86] and the saturation of R is due to the screening effects of space charge.[87] Overall, this ultrathin MoS_2 photodetector exhibits a fast response, high current on/off ratio, and high responsivity for photodetection. The higher responsivity under harmful wavelengths makes it useful for hazard warning, thereby avoiding potential damage to the eyes.

In addition to photodetection, we also characterized the glucose-sensing property. Figures 4H and 4J give a 3D schematic view and an optical image of the MoS_2-based glucose sensor, showing a large open window on the top of the PI layer and interdigital source/drain electrodes with an optimized channel length of 30 μm. This structure is designed to increase sensitivity by using a large area to absorb and immobilize the enzyme and to allow contact with the tear fluid for better glucose recognition and enhanced conductance. Here, we chose immobilized glucose oxidase (GOD) as the bio-enzyme for glucose sensing. As the standard enzyme for

biosensors, GOD has a high selectivity for glucose with fully or quasi-reversible glucose conversion, is easy to obtain, and can withstand great extremes of pH, ionic strength, and temperature; it shows good durability and stability in the long term and has reversible implantable biosensors.[88–90] As shown in Figure 4I, the glucose sensing begins with the immobilization of GOD (β-D-glucose from *Aspergillus niger*) on the MoS_2 surface.[91,92] The charge transfer process is attributed to the reaction described below, where the oxidation of glucose with GOD forms H_2O_2, which then reacts with oxygen and produces hydrogen ions (H^+) and electrons (e^-):

$$D-\text{Glucose}+H_20+O_2\overset{GOD}{\rightarrow}D-\textit{gluconic acid}+O_2+2H^++2e^-.$$

The free electrons generated by this reaction contribute to an increase of device current owing to the n-type FET behavior. Figure 4K plots the real-time response of glucose concentration versus current with a fixed bias of 5 V. Testing started with a pure phosphate-buffered saline (PBS) solution, increasing the concentration from 0.1 to 0.6 mM, which is within the same level of glucose concentration typically found in human tear fluid (mean values: 0.16 $\pm$ 0.03 mM) and diabetic tear fluid (mean values: 0.35 $\pm$ 0.04 mM).[93,94] The significant current changes indicate high sensitivity ($|\Delta R|/R_0$, e.g., 48% at 0.6 mM) proportional to the glucose levels (Figure 4L). The glucose buffer solution and artificial tears from other species were then used to test the selectivity of the glucose sensor. As shown in Figure 4M, there is no significant variation in the sensitivity of the device between these two solutions, indicating a good selectivity of for detecting glucose in the tear fluid. A variety of enzyme-based and enzyme-free glucose biosensors with different sensing materials have been reported, including metal oxides, nanoparticles, and low-dimensional materials. Table S2 summarizes and lists some of the most recent materials studied. Our results show relatively high sensitivity in the desired range of detection, while the selectivity is guaranteed by selection of the enzyme. The sensor was also tested with various concentrations of glucose in artificial tears for up to 24 h. These experiments showed no visible change in sensitivity of the sensor, indicating the high stability of the sensor (Figure S15).

Another key function of our smart contact lens is temperature sensing. Although the accurate and continuous monitoring of temperature variation of the cornea remains a challenge due to the tenderness of eyes, it can be a powerful tool to provide additional information about ocular physiology and pathology.[95]Therefore, there is high demand for smart contact lenses equipped with a low-cost, lightweight, and flexible temperature sensor. In our design, a serpentine, thin Au wire-based temperature sensor is integrated into the lens (Figures 4N and 4O). To establish the relationship between the temperature and thermal resistance of the sensor, the device was first calibrated in boiled DI water with a platinum (Pt)-based resistance temperature detector (RTD thermometer, Center 376) as a standard temperature reference. The calibration temperature spans from 30°C to 50°C, covering the full human body range and ocular surface temperature. Figure 4P displays the temperature-dependent resistance of the Au wire sensor, whose slope represents a high sensitivity of 0.94 Ω/°C and shows good linearity of the device to temperature.

The sensing properties of the device under a mechanical strain of up to 30% and Z displacement of up to 4 mm were further studied to ensure reliable operation on soft contact lenses. When the devices are stretched up to 30% of uniaxial tensile strain on the x/y axes (Figure S16) or with large displacement in the z axis (Figure S18A), the performance of the MoS_2 transistor-based photodetector and glucose sensor remains largely unchanged (i.e., relative changes of less than 8%) (Figures S17, S18C,

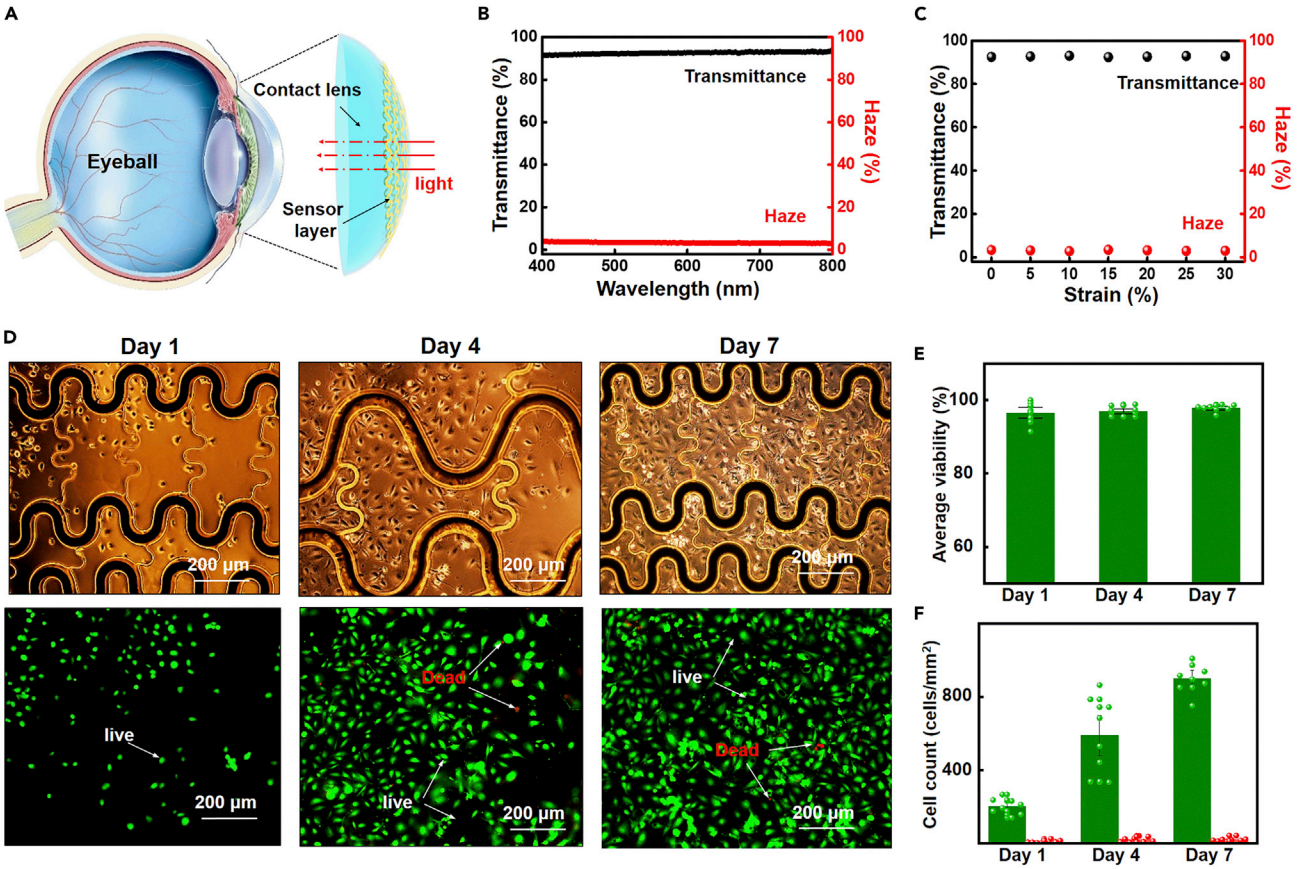

Figure 5. The optical transmittance/haze test and *in vitro* cytotoxicity test of the smart contact lens

(A) Schematic illustration of optical transmittance testing.

(B) Optical transmittance (black) and haze (red) spectra from 400 to 800 nm.

(C) Optical properties at 55 nm as a function of tensile strain up to 30%.

(D) The optical images (upper) and fluorescent images (lower) of the HUVECs at different times. In a live/dead assay, green and red fluorescence indicate living and dead cells, respectively.

(E) The average viability (percent of living cells) at days 1, 4, and 7. The percentage of living cells remained the same during the 7 days.

(F) Cell count (number of cells per area) at different times. The increasing number of living cells demonstrates cell culture reliability.

and S18D). The resistance of the Au wire-based temperature sensor also shows negligible change due to mechanical strain (Figures 4K and S18B). These results, plus the previous mechanical simulation, further indicate the strong robustness of the integrated contact lens sensor system with good sensing stability.

Characterization of the transparency and cytotoxicity of the smart contact lens

To check the transparency of the smart contact lens, we measured the optical transmittance and haze using a visible light spectrum from 400 to 800 nm (Figures 5A–5C). The contact lens exhibits high optical transmittance of ~93% and low haze of ~3% in the entire wavelength range (Figure 5B) and remains stable under a tensile strain from 0% to 30% (Figure 5C).

To confirm the biocompatibility of the lenses, *in vitro* cytotoxicity tests were performed using human umbilical vein endothelial cells (HUVECs) that were seeded and cultured for 7 days (see details in the Experimental procedures). Here HUVECs

were chosen as the test model system because of their low cost, the simple technique used for isolating them, and because they are closely related to cytotoxicity in the eye system.[96] The endothelial cells inside the blood vessels are a critical component in angiogenesis where new blood vessels are formed and are similar to the blood vessels grown from retinal blood cell in retinal neovascularization.[97] Tissue engineering has proved that it is a good candidate for prediction of ocular toxicology.[98,99] Figure 5D illustrates the liveness and mitotic behaviors of micro cells with an optical image with live cells on the substrate (upper) and corresponding fluorescence images (lower) on days 1, 4, and 7. Two fluorescence dyes—calcein AM and propidium iodide—are used in the cell assay, which stains live and dead cells to green and red colors, respectively. Figure 5E presents the average viability of over 95% at different time points, consistent with the regular cell culture results. The numbers of live (green) and dead (red) cells were obtained via the fluorescence experiments in Figure 5F. The number of live cells grows significantly throughout the duration of the experiment, while the number of dead cells remains low. These results thereby provide clear evidence that the smart contact lens is not cytotoxic to human endothelial cells, indicating good biocompatibility.

Conclusions

In summary, we have demonstrated a facile approach for fabricating multifunctional ultrathin MoS_2 transistors and a Au wire-based sensor system that could be directly incorporated onto soft contact lenses using an easy assembly method that leaves sensors exposed to directly contact the tear fluid, providing high detection sensitivity. The thin donut serpentine mesh architecture ensures strong mechanical robustness, high stretchability, and eye comfort, while maintaining high transparency. *In vitro* studies have shown that this system is fully biocompatible and nontoxic to human cells. The capabilities of the devices include detection of optical signals, glucose levels, and corneal temperature, which are essential in ocular-related research. These results provide not only an alternative solution for manufacturing advanced smart contact lenses but also a novel insight into designing other multifunctional implantable bioelectronics. In addition, our integrated contact lens sensor system and fabrication strategy allows for incorporation of other functional components, such as electrode arrays for electroretinograms,[36,37] antennas for wireless communication[25–27] and power modules (e.g., thin-film batteries/supercapacitors),[100–102] biofuel cells,[103] moisture-based energy harvesting,[104] or wireless radiofrequency[105] for future *in vivo* research.

Experimental procedures

Resource availability

Lead contact

Further information and requests for resources and reagents should be directed to and will be fulfilled by the Lead Contact, Yunlong Zhao (yunlong.zhao@surrey.ac.uk).

Materials availability

This study did not generate new unique reagents.

Data and code availability

This study did not generate/analyze any datasets/code.

Device fabrication

Gold-mediated exfoliation

A 2D bulk MoS_2 was first obtained by being peeled from a large crystal using adhesive tape (3M Blue Vinyl 471, 3M), followed by e-beam evaporation of a thin layer of

Au film (120 nm) on top of the MoS_2 bulk. A thermal release tape (3195M, Semiconductor Equipment) was then attached to the top of the Au film, transferred to a target substrate, and kept on a hot plate (120°C) until released. The target substrate was cleaned with acetone, isopropanol, and O_2 plasma. The Au layer was wet etched using a gold etchant (KI/I_2). The substrate with the MoS_2 flake can be further cleaned by immersing and rinsing in acetone at 60°C for 20 min to remove organic residues from the thermal tape.

Fabrication of devices on a rigid substrate

MoS_2 flakes were exfoliated and transferred to a SiO_2/Si substrate. The active channel was then patterned and etched by RIE (O_2/SF_6). An e-beam evaporator was used to deposit the metal layer (10 nm Ti/150 nm Au), followed by the patterning of the source and drain electrodes with photolithography.

PDMS lens mold

The elastomer and curing agent were mixed at a ratio of 10:1, followed by stirring and de-bubbling. The mixture was then poured into the gap between two concentric stainless-steel half-sphere molds and cured in a vacuum oven (StableTemp oven, Cole-Parmer) at 60°C for 30 min.

The fabrication of the smart contact lens with a "pattern-release-transfer" process is detailed in the main text.

Structure and performance characterization

Material characterization

Optical microscopy (AmScope) was used for imaging the materials and devices. Raman spectroscopy (Laser Quantum DPSS, 532 nm) was used for material verification by identification peaks associated with single-layer MoS_2. A Bruker AFM was used for measurements of the height of the MoS_2 flakes, and TEM (FEI Titan 80-300) was used to obtain a high-resolution crystal structure.

Electrical and optical measurements

The electrical measurements were conducted using a parameter analyzer (Agilent B1500A) under ambient conditions. A Panasonic NUJ6170/NU6420 light source (365 nm) was used for intensity-tunable UV light illumination. Laser light (Meade Instruments) for green and red illumination was applied for characterization of various wavelengths. The optical transmittance measurements were conducted with the transmittance of the substrate subtracted. Optical haze was calculated as the ratio of diffuse transmittance ($T_{diffuse}$) to total transmittance (T_{total}): ($T_{diffuse}/T_{total} \times 100\%$).

Strain test

The device was transferred onto a highly elastic PDMS film to perform the strain test with a tensile strain from 0% to 30%.

Preparation of the glucose solution

The glucose solution, with different concentrations, was prepared using 100 mL of PBS solution (0.1 mol/L) or artificial tear solution (Refresh Optive Advanced preservative-free lubricant eye drops) as the solvent. Different quantities of the glucose of were dissolved in the solvent to obtain glucose solution concentrations of 0.1–0.6 mM.

Mechanical FEA models

FEA simulations based on a commercial software package (Abaqus 6.14) allowed examination of the strain distribution of stretchable electronic devices with serpentine

interconnect structures. These structures, in both 3D (contact lens with a ball radius of 10 mm, thickness of 50 μm, and crown height of 4 mm) and 2D (contact lens with a thickness of 50 μm and diameter of 20 mm), were modeled by the composite shell element (S4R). The eight-node solid element modeled the eyeball, with the eyeball being regarded as a rigid body. The sensor device and contact lens were tied together using the tie constraints in Abaqus. The friction between the contact lens and the eyeball was neglected. Radial displacement and uniaxial tensile displacement (x axis and y axis tensile state) were applied to the boundary of the contact lens to explore the PI strain distributions of the serpentine interconnects, respectively. The stretchable electronic device attached to the contact lens was adhered to the eyeball by applying Z direction displacements at the boundary of the contact lens, with the eyeball fixed. The eyeball was then moved 0.5 mm along the z axis, while the boundary of the coronal contact lens was fixed. Young's modulus (E) and Poisson's ratio (v) of the materials were set as follows: PI, E_{PI} = 2.5 GPa and v_{PI} = 0.34; gold, E_{Au} = 79 GPa and v_{Au} = 0.4; MoS_2, E_{MoS2} = 330 GPa and v_{MoS2} = 0.3; PDMS contact lens, E_c = 0.5 MPa and v_c = 0.33.

Cell culture and biocompatibility studies

HUVECs cultured at 37°C and 5% CO_2 with endothelial cell basal medium-2 (EBM-2, Lonza) and an EGM-2 SingleQuots growth supplement kit (Lonza) were trypsinized using 0.25% trypsin-EDTA solution for 4 min, centrifuged at 200 rpm for 5 min, resuspended in the cell culture medium, and counted using a blood counting chamber. Then the cell suspension (containing ~5 × 10^4 cells) was seeded in a 35 mm Petri dish containing the electronic device. After adding 5 mL of fresh medium, the Petri dish was placed in an incubator at 37°C and 5% CO_2 (Forma 3131, Thermo Scientific). The cell viability of the HUVECs and the cytotoxicity of the device were identified on days 1, 4, and 7 by staining the cells with two fluorescence dyes: calcein AM and propidium iodide from Aladdin Industrial (Shanghai, China). In the experiments, the working concentrations of calcein AM and propidium iodide were 2 μM and 10 μg/mL, respectively. Cells were incubated at 37°C for ~30 min after the two dyes were added and imaged in an inverted fluorescence microscope (Olympus IX 53). The green-stained cells were living while the red-stained cells were dead. Cell viability (%) was expressed by the ratio of the number of living cells to the total number of cells, quantified using ImageJ software. The experiments were repeated at least three times.

Supplemental information

Supplemental information can be found online at https://doi.org/10.1016/j.matt.2020.12.002.

Acknowledgments

We would like to thank GW Nanofabrication and Imaging Center for providing the nanofabrication facilities. This work was partially carried out at the USTC Center for Micro and Nanoscale Research and Fabrication. We also appreciate the support from the UK National Measurement System and ISCF Measurement Fellowship.

Author contributions

D.Y. conceived the concept and designed the experiments. S.G. carried out the main experiments. K.W. performed the mechanism analysis. Y.Z. supervised the research process. S.G., D.Y., and Y.Z. analyzed the data and wrote the manuscript. C.L., H.W., W.D., and C.W. carried out the biological experiments. Z.S. and S.Z collected the temperature sensor and glucose sensor data. D.X. performed the

optical transmittance test. M.E.Z. and F.A.C. provided advice on the concept. All authors contributed to the discussion and provided feedback on the manuscript.

Declaration of interests

The authors declare no competing interests.

Received: July 27, 2020
Revised: October 28, 2020
Accepted: December 3, 2020
Published: December 30, 2020

References

1. Morales-Narváez, E., and Dincer, C. (2020). The impact of biosensing in a pandemic outbreak: COVID-19. Biosens. Bioelectron. 112274, https://doi.org/10.1016/j.bios.2020.112274.

2. Da Silva Neves, M.M.P., González-García, M.B., Hernandez-Santos, D., and Fanjul-Bolado, P. (2018). Future trends in the market for electrochemical biosensing. Curr. Opin. Electrochem. *10*, 107–111.

3. Mück, J.E., Ünal, B., Butt, H., and Yetisen, A.K. (2019). Market and patent analyses of wearables in medicine. Trends Biotechnol. *37*, 563–566.

4. Kim, J., Campbell, A.S., de Ávila, B.E.-F., and Wang, J. (2019). Wearable biosensors for healthcare monitoring. Nat. Biotechnol. *37*, 389–406.

5. Birmingham, K., Gradinaru, V., Anikeeva, P., Grill, W.M., Pikov, V., McLaughlin, B., Pasricha, P., Weber, D., Ludwig, K., and Famm, K. (2014). Bioelectronic medicines: a research roadmap. Nat. Rev. Drug Discov. *13*, 399–400.

6. An, B.W., Shin, J.H., Kim, S.Y., Kim, J., Ji, S., Park, J., Lee, Y., Jang, J., Park, Y.G., Cho, E., et al. (2017). Smart sensor systems for wearable electronic devices. Polymers (Basel) *9*, 303.

7. Jiang, Y., and Tian, B. (2018). Inorganic semiconductor biointerfaces. Nat. Rev. Mater. *3*, 473–490.

8. Rogers, J.A., Ghaffari, R., and Kim, D.-H. (2016). Stretchable Bioelectronics for Medical Devices and Systems (Springer).

9. Someya, T., Bao, Z., and Malliaras, G.G. (2016). The rise of plastic bioelectronics. Nature *540*, 379–385.

10. Yetisen, A.K., Martinez-Hurtado, J.L., Ünal, B., Khademhosseini, A., and Butt, H. (2018). Wearables in medicine. Adv. Mater. *30*, 1706910.

11. Yu, Y., Nyein, H.Y.Y., Gao, W., and Javey, A. (2020). Flexible electrochemical bioelectronics: the rise of in situ bioanalysis. Adv. Mater. *32*, 1902083.

12. Zhang, A., and Lieber, C.M. (2016). Nano-bioelectronics. Chem. Rev. *116*, 215–257.

13. Luo, S., Wu, S., Xu, J., Zhang, X., Zou, L., Yao, R., et al. (2020). Osteogenic differentiation of BMSCs on MoS_2 composite nanofibers with different cell seeding densities. Appl. Nanosci. *10*, 3703–3716, https://doi.org/10.1007/s13204-020-01473-0.

14. Bhavnani, S.P., Narula, J., and Sengupta, P.P. (2016). Mobile technology and the digitization of healthcare. Eur. Heart J. *37*, 1428–1438.

15. Patel, S.R., and Lieber, C.M. (2019). Precision electronic medicine in the brain. Nat. Biotechnol. *37*, 1007–1012.

16. Yang, J.C., Mun, J., Kwon, S.Y., Park, S., Bao, Z., and Park, S. (2019). Electronic skin: recent progress and future prospects for skin-attachable devices for health monitoring, robotics, and prosthetics. Adv. Mater. *31*, 1904765.

17. Yu, K.-H., Beam, A.L., and Kohane, I.S. (2018). Artificial intelligence in healthcare. Nat. Biomed. Eng. *2*, 719–731.

18. Zhang, X. (2019). Nanowires pin neurons: "a nano Moon Landing". Matter *1*, 560–562.

19. Kim, J., Cha, E., and Park, J.U. (2020). Recent advances in smart contact lenses. Adv. Mater. Tech. *5*, 1900728.

20. Bennett, E.S., and Henry, V.A. (2019). Clinical Manual of Contact Lenses (Lippincott Williams & Wilkins).

21. Farandos, N.M., Yetisen, A.K., Monteiro, M.J., Lowe, C.R., and Yun, S.H. (2015). Contact lens sensors in ocular diagnostics. Adv. Healthc. Mater. *4*, 792–810.

22. Moreddu, R., Vigolo, D., and Yetisen, A.K. (2019). Contact lens technology: from fundamentals to applications. Adv. Healthc. Mater. *8*, 1900368.

23. Tseng, R.C., Chen, C.-C., Hsu, S.-M., and Chuang, H.-S. (2018). Contact-lens biosensors. Sensors *18*, 2651.

24. Kownacka, A.E., Vegelyte, D., Joosse, M., Anton, N., Toebes, B.J., Lauko, J., Buzzacchera, I., Lipinska, K., Wilson, D.A., Geelhoed-Duijvestijn, N., and Wilson, C.J. (2018). Clinical evidence for use of a noninvasive biosensor for tear glucose as an alternative to painful finger-prick for diabetes management utilizing a biopolymer coating. Biomacromolecules *19*, 4504–4511.

25. Chu, M., Iguchi, S., Miyajima, K., Arakawa, T., Kudo, H., and Mitsubayashi, K. (2011). Development of a soft contact-lens biosensor for in-vivo tear glucose monitoring. In 5th European Conference of the International Federation for Medical and Biological Engineering, A. Jobbágy, ed. (Springer), pp. 1007–1010.

26. Kim, J., Kim, M., Lee, M.-S., Kim, K., Ji, S., Kim, Y.-T., Park, J., Na, K., Bae, K.-H., and Kim, H.K. (2017). Wearable smart sensor systems integrated on soft contact lenses for wireless ocular diagnostics. Nat. Commun. *8*, 1–8.

27. Kim, S.-K., Koo, J., Lee, G.-H., Jeon, C., Mok, J.W., Mun, B.H., Lee, K.J., Kamrani, E., Joo, C.-K., and Shin, S. (2020). Wireless smart contact lens for diabetic diagnosis and therapy. Sci. Adv. *6*, eaba3252.

28. Park, J., Kim, J., Kim, S.-Y., Cheong, W.H., Jang, J., Park, Y.-G., Na, K., Kim, Y.-T., Heo, J.H., and Lee, C.Y. (2018). Soft, smart contact lenses with integrations of wireless circuits, glucose sensors, and displays. Sci. Adv. *4*, eaap9841.

29. Chu, M.X., Miyajima, K., Takahashi, D., Arakawa, T., Sano, K., Sawada, S.-i., Kudo, H., Iwasaki, Y., Akiyoshi, K., and Mochizuki, M. (2011). Soft contact lens biosensor for in situ monitoring of tear glucose as non-invasive blood sugar assessment. Talanta *83*, 960–965.

30. Lee, S.H., Cho, Y.C., and Choy, Y.B. (2019). Noninvasive self-diagnostic device for tear collection and glucose measurement. Sci. Rep. *9*, 1–8.

31. Matz, K., Keresztes, K., Tatschl, C., Nowotny, M., Dachenhausen, A., Brainin, M., and Tuomilehto, J. (2006). Disorders of glucose metabolism in acute stroke patients: an underrecognized problem. Diabetes Care *29*, 792–797.

32. Koponen, H., Kautiainen, H., Leppänen, E., Mäntyselkä, P., and Vanhala, M. (2015). Association between suicidal behaviour and impaired glucose metabolism in depressive disorders. BMC Psychiatry *15*, 163.

33. Petersen, M.C., Vatner, D.F., and Shulman, G.I. (2017). Regulation of hepatic glucose metabolism in health and disease. Nat. Rev. Endocrinol. *13*, 572–587.

34. Fabiani, C., Li Voti, R., Rusciano, D., Mutolo, M.G., and Pescosolido, N. (2016). Relationship between corneal temperature and intraocular pressure in healthy individuals: a clinical thermographic analysis. J. Ophthalmol. *2016*, 3076031, https://doi.org/10.1155/2016/3076031.

35. Tan, L.L., Sanjay, S., and Morgan, P.B. (2016). Static and dynamic measurement of ocular surface temperature in dry eyes. J. Ophthalmol. *2016*, 7285132.

36. Kawali, A.A. (2016). Thermography in ocular inflammation. Indian J. Radiol. Imaging *23*, 281–283.

37. Hong, G., Fu, T.-M., Qiao, M., Viveros, R.D., Yang, X., Zhou, T., Lee, J.M., Park, H.-G., Sanes, J.R., and Lieber, C.M. (2018). A method for single-neuron chronic recording from the retina in awake mice. Science *360*, 1447–1451.

38. Yin, R., Xu, Z., Mei, M., Chen, Z., Wang, K., Liu, Y., Tang, T., Priydarshi, M.K., Meng, X., and Zhao, S. (2018). Soft transparent graphene contact lens electrodes for conformal full-cornea recording of electroretinogram. Nat. Commun. *9*, 1–11.

39. Vásquez Quintero, A., Verplancke, R., De Smet, H., and Vanfleteren, J. (2017). Stretchable electronic platform for soft and smart contact lens applications. Adv. Mater. Tech. *2*, 1700073.

40. Alipour, F., Khaheshi, S., Soleimanzadeh, M., Heidarzadeh, S., and Heydarzadeh, S. (2017). Contact lens-related complications: a review. J. Ophthalmic Vis. Res. *12*, 193.

41. Jariwala, D., Sangwan, V.K., Lauhon, L.J., Marks, T.J., and Hersam, M.C. (2014). Emerging device applications for semiconducting two-dimensional transition metal dichalcogenides. ACS Nano *8*, 1102–1120.

42. Chhowalla, M., Shin, H.S., Eda, G., Li, L.-J., Loh, K.P., and Zhang, H. (2013). The chemistry of two-dimensional layered transition metal dichalcogenide nanosheets. Nat. Chem. *5*, 263–275.

43. Tan, C., and Zhang, H. (2015). Two-dimensional transition metal dichalcogenide nanosheet-based composites. Chem. Soc. Rev. *44*, 2713–2731.

44. Wang, Q.H., Kalantar-Zadeh, K., Kis, A., Coleman, J.N., and Strano, M.S. (2012). Electronics and optoelectronics of two-dimensional transition metal dichalcogenides. Nat. Nanotechnol. *7*, 699–712.

45. Choi, C., Choi, M.K., Liu, S., Kim, M.S., Park, O.K., Im, C., Kim, J., Qin, X., Lee, G.J., and Cho, K.W. (2017). Human eye-inspired soft optoelectronic device using high-density MoS_2-graphene curved image sensor array. Nat. Commun. *8*, 1–11.

46. Jiang, N., Montelongo, Y., Butt, H., and Yetisen, A.K. (2018). Microfluidic contact lenses. Small *14*, 1704363.

47. Filipe, H., Bozukova, D., Pimenta, A., Vieira, A., Alves, P., Coimbra, P., Guiomar, A., Gil, M., Mata, J., and Serro, A. (2015). Surface modification of intraocular lenses towards controlled drug delivery. Acta Ophthalmol. *93*, https://doi.org/10.1111/j.1755-3768.2015.0561.

48. Kamei, T., and Wada, T. (2006). Contact-lens type of micromachined hydrogenated amorphous Si fluorescence detector coupled with microfluidic electrophoresis devices. Appl. Phys. Lett. *89*, 114101.

49. Radisavljevic, B., Radenovic, A., Brivio, J., Giacometti, V., and Kis, A. (2011). Single-layer MoS_2 transistors. Nat. Nanotechnol. *6*, 147.

50. Lopez-Sanchez, O., Lembke, D., Kayci, M., Radenovic, A., and Kis, A. (2013). Ultrasensitive photodetectors based on monolayer MoS_2. Nat. Nanotechnol. *8*, 497–501.

51. Shokri, A., and Salami, N. (2016). Gas sensor based on MoS_2 monolayer. Sens. Actuat. B Chem. *236*, 378–385.

52. Kim, T.H., Kim, Y.H., Park, S.Y., Kim, S.Y., and Jang, H.W. (2017). Two-dimensional transition metal disulfides for chemoresistive gas sensing: perspective and challenges. Chemosensors *5*, 15.

53. Jariwala, D., Sangwan, V.K., Late, D.J., Johns, J.E., Dravid, V.P., Marks, T.J., Lauhon, L.J., and Hersam, M.C. (2013). Band-like transport in high mobility unencapsulated single-layer MoS_2 transistors. Appl. Phys. Lett. *102*, 173107.

54. Cho, B., Hahm, M.G., Choi, M., Yoon, J., Kim, A.R., Lee, Y.-J., Park, S.-G., Kwon, J.-D., Kim, C.S., and Song, M. (2015). Charge-transfer-based gas sensing using atomic-layer MoS_2. Sci. Rep. *5*, 8052.

55. Lee, G.-H., Yu, Y.-J., Cui, X., Petrone, N., Lee, C.-H., Choi, M.S., Lee, D.-Y., Lee, C., Yoo, W.J., and Watanabe, K. (2013). Flexible and transparent MoS_2 field-effect transistors on hexagonal boron nitride-graphene heterostructures. ACS Nano *7*, 7931–7936.

56. Velusamy, D.B., Kim, R.H., Cha, S., Huh, J., Khazaeinezhad, R., Kassani, S.H., Song, G., Cho, S.M., Cho, S.H., and Hwang, I. (2015). Flexible transition metal dichalcogenide nanosheets for band-selective photodetection. Nat. Commun. *6*, 1–11.

57. Guo, S., Yang, D., Zhang, S., Dong, Q., Li, B., Tran, N., Li, Z., Xiong, Y., and Zaghloul, M.E. (2019). Development of a cloud-based epidermal $MoSe_2$ device for hazardous gas sensing. Adv. Funct. Mater. *29*, 1900138.

58. Splendiani, A., Sun, L., Zhang, Y., Li, T., Kim, J., Chim, C.-Y., Galli, G., and Wang, F. (2010). Emerging photoluminescence in monolayer MoS_2. Nano Lett. *10*, 1271–1275.

59. Bertolazzi, S., Brivio, J., and Kis, A. (2011). Stretching and breaking of ultrathin MoS_2. ACS Nano *5*, 9703–9709.

60. Plechinger, G., Mann, J., Preciado, E., Barroso, D., Nguyen, A., Eroms, J., Schueller, C., Bartels, L., and Korn, T. (2014). A direct comparison of CVD-grown and exfoliated MoS_2 using optical spectroscopy. Semiconductor Sci. Technol. *29*, 064008.

61. Chen, X., Park, Y.J., Kang, M., Kang, S.-K., Koo, J., Shinde, S.M., Shin, J., Jeon, S., Park, G., and Yan, Y. (2018). CVD-grown monolayer MoS_2 in bioabsorbable electronics and biosensors. Nat. Commun. *9*, 1–12.

62. Kim, T.-Y., Song, Y., Cho, K., Amani, M., Ahn, G.H., Kim, J.-K., Pak, J., Chung, S., Javey, A., and Lee, T. (2017). Analysis of the interface characteristics of CVD-grown monolayer MoS_2 by noise measurements. Nanotechnology *28*, 145702.

63. Desai, S.B., Madhvapathy, S.R., Amani, M., Kiriya, D., Hettick, M., Tosun, M., Zhou, Y., Dubey, M., Ager, J.W., III, and Chrzan, D. (2016). Gold-mediated exfoliation of ultralarge optoelectronically-perfect monolayers. Adv. Mater. *28*, 4053–4058.

64. Kim, D.-H., Lu, N., Ma, R., Kim, Y.-S., Kim, R.-H., Wang, S., Wu, J., Won, S.M., Tao, H., and Islam, A. (2011). Epidermal electronics. Science *333*, 838–843.

65. Su, Y., Ping, X., Yu, K.J., Lee, J.W., Fan, J.A., Wang, B., et al. (2017). In-plane deformation mechanics for highly stretchable electronics. Adv. Mater. *29*, 1604989, https://doi.org/10.1002/adma.201604989.

66. Hwang, S.-W., Lee, C.H., Cheng, H., Jeong, J.-W., Kang, S.-K., Kim, J.-H., Shin, J., Yang, J., Liu, Z., and Ameer, G.A. (2015). Biodegradable elastomers and silicon nanomembranes/nanoribbons for stretchable, transient electronics, and biosensors. Nano Lett. *15*, 2801–2808.

67. An, H.B., Chen, L.Z., Liu, X.J., Zhao, B., Ma, D.L., and Wu, Z.G. (2018). A method of manufacturing microfluidic contact lenses by using irreversible bonding and thermoforming. J. Micromech. Microeng. *28*, 105008.

68. Chen, J.S., Liu, T.Y., Tsou, H.M., Ting, Y.S., Tseng, Y.Q., and Wang, C.H. (2017). Biopolymer brushes grown on PDMS contact lenses by in situ atmospheric plasma-induced polymerization. J. Polym. Res. *24*, 69.

69. Musgrave, C.S.A., and Fang, F. (2019). Contact lens materials: a materials science perspective. Materials (Basel) *12*, 261.

70. Marc, P., Wolf, G.B.S.-B., and Hunziker, P. (2018). PDMS with designer functionalities—properties, modifications strategies, and applications. Prog. Polym. Sci. *83*, 97–134.

71. Quintana-Puebla, A., and Paranjape, M. (2020). Systematic characterization of hydrophilized polydimethylsiloxane. J. Microelectromechanical Syst. *29*, 1216–1224.

72. Jeong, S., Shin, H.-Y., Shin, R., Jo, W., Yoon, S., and Rübhausen, M. (2015). Raman scattering studies of the lattice dynamics in layered MoS_2. J. Korean Phys. Soc. *66*, 1575–1580.

73. Bao, W., Cai, X., Kim, D., Sridhara, K., and Fuhrer, M.S. (2013). High mobility ambipolar MoS_2 field-effect transistors: substrate and dielectric effects. Appl. Phys. Lett. *102*, 042104.

74. Radisavljevic, B., and Kis, A. (2013). Mobility engineering and a metal–insulator transition in monolayer MoS_2. Nat. Mater. *12*, 815–820.

75. Yu, Z., Ong, Z., Li, S., Xu, J., Zhang, G., Zhang, Y., Shi, Y., and Wang, X. (2017). Analyzing the carrier mobility in transition-metal dichalcogenide MoS_2 field-effect transistors. Adv. Funct. Mater. *18*, 1604093.

76. Wang, H.H., Su, C.H., Wu, Y.J., Lin, C.A.J., Lee, C.H., Shen, J.L., Chan, W.H., Chang, W.H., and Yeh, H.I. (2012b). Application of gold in biomedicine: past, present and future. Int. J. Gerontol. *6*, 1–4.

77. Menard, E., Lee, K., Khang, D.-Y., Nuzzo, R.G., and Rogers, J.A. (2004). A printable form of silicon for high performance thin film transistors on plastic substrates. Appl. Phys. Lett. *84*, 5398–5400.

78. Verplancke, R., Bossuyt, F., Cuypers, D., and Vanfleteren, J. (2011). Thin-film stretchable electronics technology based on meandering interconnections: fabrication and mechanical performance. J. Micromechanics Microengineering *22*, 015002.

79. Huang, X., Liu, Y., Kong, G.W., Seo, J.H., Ma, Y., Jang, K.-I., Fan, J.A., Mao, S., Chen, Q., and Li, D. (2016). Epidermal radio frequency electronics for wireless power transfer. Microsystems Nanoengineering *2*, 1–9.

80. Xu, S., Zhang, Y., Cho, J., Lee, J., Huang, X., Jia, L., Fan, J.A., Su, Y., Su, J., and Zhang, H. (2013). Stretchable batteries with self-similar serpentine interconnects and integrated wireless recharging systems. Nat. Commun. *4*, 1–8.

81. Jang, K.-I., Li, K., Chung, H.U., Xu, S., Jung, H.N., Yang, Y., Kwak, J.W., Jung, H.H., Song, J., and Yang, C. (2017). Self-assembled three dimensional network designs for soft electronics. Nat. Commun. *8*, 1–10.

82. Youssef, P.N., Sheibani, N., and Albert, D.M. (2011). Retinal light toxicity. Eye (London, England) *25*, 1–14.

83. Young, R.W. (1994). The family of sunlight-related eye diseases. Optom. Vis. Sci. *71*, 125–144.

84. Rozanowska, M.B. (2012). Light-induced damage to the retina: current understanding of the mechanisms and unresolved questions: a symposium-in-print. Photochem. Photobiol. *88*, 1303–1308.

85. De Fazio, D., Goykhman, I., Yoon, D., Bruna, M., Eiden, A., Milana, S., Sassi, U., Barbone, M., Dumcenco, D., and Marinov, K. (2016). High responsivity, large-area graphene/MoS_2 flexible photodetectors. ACS Nano *10*, 8252–8262.

86. Saenz, G.A., Karapetrov, G., Curtis, J., and Kaul, A.B. (2018). Ultra-high photoresponsivity in suspended metal-semiconductor-metal mesoscopic multilayer MoS_2 broadband detector from UV-to-IR with low Schottky barrier contacts. Sci. Rep. *8*, 1276.

87. Mueller, T., Xia, F., and Avouris, P. (2010). Graphene photodetectors for high-speed optical communications. Nat. Photon. *4*, 297.

88. Bankar, S.B., Bule, M.V., Singhal, R.S., and Ananthanarayan, L. (2009). Glucose oxidase—an overview. Biotechnol. Adv. *27*, 489–501.

89. Rinky Sha, T.K.B. (2020). MoS_2-based nanosensors in biomedical and environmental monitoring applications. Electrochimica Acta *349*, 136370.

90. Tim Bobrowski, W.S. (2018). Long-term implantable glucose biosensors. Curr. Opin. Electrochemistry *10*, 112–119.

91. Shan, J., Li, J., Chu, X., Xu, M., Jin, F., Wang, X., Ma, L., Fang, X., Wei, Z., and Wang, X. (2018). High sensitivity glucose detection at extremely low concentrations using a MoS_2-based field-effect transistor. RSC Adv. *8*, 7942–7948.

92. Wu, S., Huang, H., Shang, M., Du, C., Wu, Y., and Song, W. (2017). High visible light sensitive MoS_2 ultrathin nanosheets for photoelectrochemical biosensing. Biosens. Bioelectron. *92*, 646–653.

93. Lane, J.D., Krumholz, D.M., Sack, R.A., and Morris, C. (2006). Tear glucose dynamics in diabetes mellitus. Curr. Eye Res. *31*, 895–901.

94. Sen, D., and Sarin, G. (1980). Tear glucose levels in normal people and in diabetic patients. Br. J. Ophthalmol. *64*, 693–695.

95. Purslow, C., and Wolffsohn, J.S. (2005). Ocular surface temperature: a review. Eye Contact Lens *31*, 117–123.

96. Cao, Y., Gong, Y., Liu, L., Zhou, Y., Fang, X., Zhang, C., Li, Y., and Li, J. (2017). The use of human umbilical vein endothelial cells (HUVECs) as an in vitro model to assess the toxicity of nanoparticles to endothelium: a review. J. Appl. Toxicol. *37*, 1359–1369.

97. Medina-Leyte, D.J., Domínguez-Pérez, M., Mercado, I., Villarreal-Molina, M.T., and Jacobo-Albavera, L. (2020). Use of human umbilical vein endothelial cells (HUVEC) as a model to study cardiovascular disease: a review. Appl. Sci. *10*, 938.

98. Kumar, R., Harris-Hooker, S., Kumar, R., and Sanford, G. (2011). Co-culture of retinal and endothelial cells results in the modulation of genes critical to retinal neovascularization. Vasc. Cell *3*, 27.

99. Ronkko, S., Vellonen, K.S., Jarvinen, K., Toropainen, E., and Urtti, A. (2016). Human corneal cell culture models for drug toxicity studies. Drug Deliv. Transl Res. *6*, 660–675.

100. Lee, H., Kim, S., Kim, K.-B., and Choi, J.-W. (2018). Scalable fabrication of flexible thin-film batteries for smart lens applications. Nano Energy *53*, 225–231.

101. Park, J., Ahn, D.B., Kim, J., Cha, E., Bae, B.-S., Lee, S.-Y., and Park, J.-U. (2019). Printing of wirelessly rechargeable solid-state supercapacitors for soft, smart contact lenses with continuous operations. Sci. Adv. *5*, eaay0764.

102. Nasreldin, M., Delattre, R., Ramuz, M., Lahuec, C., Djenizian, T., and de Bougrenet de la Tocnaye, J.-L. (2019). Flexible micro-battery for powering smart contact lens. Sensors *19*, 2062.

103. Reid, R.C., Minteer, S.D., and Gale, B.K. (2015). Contact lens biofuel cell tested in a synthetic tear solution. Biosens. Bioelectron. *68*, 142–148.

104. Liu, X., Gao, H., Ward, J.E., Liu, X., Yin, B., Fu, T., Chen, J., Lovley, D.R., and Yao, J. (2020). Power generation from ambient humidity using protein nanowires. Nature *578*, 550–554.

105. Borges, L.M., Chávez-Santiago, R., Barroca, N., Velez, F.J., and Balasingham, I. (2015). Radio-frequency energy harvesting for wearable sensors. Healthc. Technol. Lett. *2*, 22–27.